Available online at www.sciencedirect.com
SCIENCE DIRECT®
Journal of Colloid and Interface Science 269 (2004) 72–78
JOURNAL OF Colloid and Interface Science
www.elsevier.com/locate/jcis

Orientational defects near colloidal particles in a nematic liquid crystal

James J. Feng [a,*] and Chixing Zhou [b]

[a] *The Levich Institute for Physicochemical Hydrodynamics, City College of the City University of New York, New York, NY 10031, USA*
[b] *Department of Polymer Science and Engineering, Shanghai Jiao Tong University, Shanghai 200240, China*

Received 21 March 2003; accepted 25 August 2003

Abstract

We study the interaction between a surface-anchoring colloidal particle and a liquid-crystalline host, and in particular the formation of orientational defects near the particle. A mean-field theory based on the nonlocal Marrucci–Greco nematic potential is used to represent molecular interactions in an inhomogeneous orientational field. An evolution equation for the molecular configuration tensor is solved numerically whose steady state minimizes the total free energy of the system. With strong homeotropic anchoring on the particle surface, three types of solutions may appear depending on initial conditions and particle size: Saturn rings, satellite point defects, and polar rings. The Saturn ring remains stable on micrometer-sized particles, contrary to previous calculations but consistent with experiments. A phase diagram is constructed for the three regimes. Based on the free energy, the most stable state is the Saturn ring for smaller particles and the satellite defect for larger ones.

Keywords: Liquid crystal; Surface anchoring; Nematic suspension; Self-assembly

1. Introduction

When solid or liquid particles are introduced into a nematic host, they tend to self-assemble into regular patterns [1]. The nematic molecules prefer to orient at a certain angle on the particle surface, e.g., perpendicularly in the so-called homeotropic anchoring. Thus, the anchoring direction on particle surfaces will come into conflict with the far-field orientation. It is believed that the resulting defects play critical roles in mediating the interaction between particles and the formation of novel microstructures [1,2]. Most theoretical work to date relies on a linear elasticity theory for liquid crystals known as the Frank theory [3–5]. It assumes that the molecular orientation distribution is uniaxial about the director **n**, and that spatial variation of **n** is mild. Both assumptions break down at defects where the **n** field becomes singular. Traditionally, this difficulty is circumvented by applying the theory outside the defect core and assigning a size and an effective energy to the core. Thus, defects cannot be treated in a self-consistent way. Our work overcomes this difficulty by using a mean-field theory based on a nonlocal nematic potential that describes the molecular interaction in the nematic subject to distortion. Given an initial configuration and anchoring conditions on the particle, the orientational field relaxes to a steady state with defects near the particle. This steady state represents a local minimum of the total free energy, which comprises a molecular and a distortional component. Numerical results show the familiar satellite and Saturn ring defects. Contrary to previous calculations but consistent with experiments, the Saturn ring is predicted to remain stable on supra-micrometer particles. In addition, our theory reveals a new metastable configuration termed the polar ring. Finally, the mean-field theory allows us to compute the core energy and determine the relative stability of the three types of defects.

Following is a brief summary of prior studies of defects near a colloidal particle with strong homeotropic anchoring. Three methods have been used to minimize the Frank elastic energy: minimization among a family of ansatz director fields [2,6]; numerical solution of the Euler–Lagrange equation [4,5]; and a Monte Carlo method on a lattice [7]. All produce similar results showing the Saturn ring and satellite defect as stable configurations. Owing to the theory's inherent inability to describe defect cores, it cannot determine in a self-contained way which state has lower energy [7]. Assuming a "melted" core with a 10-nm radius and a constant energy density, Stark [4,5] estimated the energy of a defect

* Corresponding author.
E-mail address: feng@ccny.cuny.edu (J.J. Feng).

0021-9797/$ – see front matter
doi:10.1016/j.jcis.2003.08.048

ring and predicted the Saturn ring to be unstable on particles with radius $R > 720$ nm. This seems to contradict the observations of Gu and Abbott [8] of the Saturn ring on particles 40 μm in diameter. As a more sophisticated phenomenology, a Landau–de Gennes energy has been minimized [9,10] to predict that the preferred state is a Saturn ring for smaller particles and a satellite defect for larger ones. Finally, molecular dynamics (MD) simulations [11,12] have also shown the two configurations, albeit for tiny particle sizes. The Saturn ring obtains for particles with a radius smaller than roughly 15 molecular widths, and gives way to satellite defects for larger particles. The transition resembles experimental observations and calculations based on the Frank theory, but there is a discrepancy of several orders of magnitude in length scale.

The purpose of the present work is to provide a clear and self-consistent picture for the relative stability of various defect patterns near a strongly anchoring spherical particle. This is achieved via a mean-field theory due to Marrucci and Greco [13], which will be briefly described below.

2. Theoretical model and numerical method

Marrucci and Greco [13] derived a potential energy for interaction among rigid-rod molecules in a distorted nematic material. The spatial distortion, represented by variation of the orientation distribution function $\Psi(\mathbf{u};\mathbf{r})$, requires consideration of nonlocal interactions between two molecules some distance apart. This contrasts the local interaction in homogeneous nematics that underlies classical potential energies due to Onsager [14] and Maier and Saupe [15]. For a test molecule oriented along the unit vector $\mathbf{u}$ at position $\mathbf{r}$, Marrucci and Greco [13] delineated an interaction region V enveloping the test molecule (Fig. 1). By expanding $\Psi(\mathbf{u};\mathbf{r}+\boldsymbol{\rho})$ in a Taylor series for the small distance $\boldsymbol{\rho}$, and spatially averaging the interaction energy of all molecules inside a spherical V, Marrucci and Greco obtained the nematic potential energy

$$U_{\mathrm{MG}}(\mathbf{u}) = -\frac{3}{2}UkT(\mathbf{A}+\mathcal{L}^2\nabla^2\mathbf{A}):\mathbf{uu}, \tag{1}$$

where U is a constant representing the strength of intermolecular forces and can be related to the geometry and concentration of rigid-rod molecules [16], k is the Boltzmann constant, and T is the absolute temperature. $\mathbf{A}(\mathbf{r}) = \int \Psi(\mathbf{u};\mathbf{r})\mathbf{uu}\,d\mathbf{u} = \langle\mathbf{uu}\rangle$ is the configuration tensor. The interaction length $\mathcal{L} \sim V^{1/3}$ is the only free parameter in the theory. For p-azoxyanisole, $\mathcal{L}$ should be on the order of $1/10$ of the molecular length L for Eq. (1) to predict reasonable values for the elastic constants [13]. Equation (1) can be seen as a molecularly based generalization of the Maier–Saupe potential [15]. In the limit of weak spatial variations, it reduces to the Frank elastic energy with one elastic constant $K = 3\nu kTUS_{\mathrm{eq}}^2\mathcal{L}^2$, ν being the number density of the molecules and S_{eq} the equilibrium order parameter. A more general version of the Marrucci–Greco energy, based on a nonspherical V that accounts for the molecular length, allows three unequal elastic constants [13], but we will not concern ourselves with elastic anisotropy in this paper.

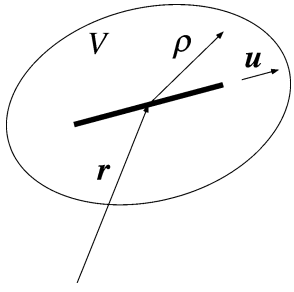

Fig. 1. The interaction volume V around a test molecule used by Marrucci and Greco [13] in deriving a nonlocal nematic potential.

Using Eq. (1), an evolution equation can be derived for $\mathbf{A}$ subject to flow, Brownian motion and nematic interactions [17,18],

$$\begin{aligned}\frac{\partial\mathbf{A}}{\partial t} &+ \mathbf{v}\cdot\nabla\mathbf{A} - \boldsymbol{\kappa}^T\cdot\mathbf{A} - \mathbf{A}\cdot\boldsymbol{\kappa}\\ &= -6D_r\left(\mathbf{A}-\frac{\boldsymbol{\delta}}{3}\right) + 6D_rU\left(\mathbf{A}\cdot\mathbf{A} - \mathbf{A}:\langle\mathbf{uuuu}\rangle\right)\\ &\quad - 2\boldsymbol{\kappa}:\langle\mathbf{uuuu}\rangle + 3D_rU\mathcal{L}^2\left(\nabla^2\mathbf{A}\cdot\mathbf{A} + \mathbf{A}\cdot\nabla^2\mathbf{A}\right.\\ &\quad \left. - 2\nabla^2\mathbf{A}:\langle\mathbf{uuuu}\rangle\right),\end{aligned} \tag{2}$$

where $\mathbf{v}$ is the velocity and $\boldsymbol{\kappa}$ its gradient, D_r is the rotational diffusivity, and $\boldsymbol{\delta}$ is the unit tensor. The fourth momentum tensor $\langle\mathbf{uuuu}\rangle = \int\Psi\mathbf{uuuu}\,d\mathbf{u}$ will be related to $\mathbf{A}$ via the Bingham closure [19,20], which assumes a special form for the orientation distribution function $\Psi(\mathbf{u})$. By setting the flow terms to zero, this equation describes the annealing of orientation in a distorted nematic driven by the interplay between relaxation of the molecular orientation distribution and spatial distortion. The former, represented by the first two brackets on the right hand side of Eq. (2), is the same as gives rise to molecular viscoelasticity in flexible polymers [16], while the latter, represented by the Laplacian terms, is a mean-field generalization of Frank elasticity. This evolution decreases the free energy of the system, and the final steady state is its minimizer [21]. The Bingham closure becomes exact in equilibrium as the Boltzmann distribution with the energy of Eq. (1) has the exact Bingham form. Starting from an initial condition, we use this annealing process to compute the stable orientation field near particles embedded in a nematic. Of course, there may exist multiple metastable states, and the local energy minimum reached in this procedure will depend on the initial conditions.

The mean-field theory avoids the difficulties of Frank elasticity by employing a tensorial description of the molecular orientation. This could have been accomplished by using the classical Laudau–de Gennes expansion [22]. We prefer the Marrucci–Greco energy because of the fundamental limitations of the Landau–de Gennes approach, as

carefully critiqued by Greco [23]. First, the expansion represents "the free energy density in the isotropic phase" due to short-range order [24] and is valid only in the neighborhood of the isotropic state. Katriel et al. [25] showed that the expansion, with coefficients evaluated from a molecular theory, fails to converge for moderate-order parameters typical of real nematics. Second, the coefficients of the expansion are to be fitted to the isotropic state and remain constant. This is inadequate if the material is strongly distorted as near defects [26]. Finally, a constitutive theory for liquid-crystalline polymers, derived using the Landau–de Gennes energy through a Poisson bracket procedure, gives rise to nonphysical maxima in the shear and normal stresses [27]. In comparison, the Marrucci–Greco energy has a molecular basis and does not contain many phenomenological coefficients. Of course, MD simulations retain even more molecular details such as spatial variations of density. But they are limited by small sample sizes and nanoscopic length scales [12]. An additional advantage of the mean-field theory is that it is easily extendable to dynamic problems in complex geometry, such as are relevant, for example, to processing flows of liquid-crystalline polymers [18,28]. A limitation of the mean-field theory is that the Taylor expansion used in deriving Eq. (1) requires that spatial variations be small over the length $\mathcal{L}$. This is not very restrictive since it allows resolution down to the molecular length $L \sim 10\mathcal{L}$.

Details of the setup of the problem are as follows. A sphere with strong homeotropic anchoring is placed in a nematic which is otherwise uniformly oriented along the z direction. By assuming axisymmetry about z and using spherical coordinates, our computation domain lies in the $r\theta$ plane: $R < r < R_\infty$, $0 < \theta < \pi$ (Fig. 2). In all cases computed, the defect and most of the distortion occur near the particle, and it is sufficient to set the outer edge of the domain at $R_\infty = 3R$; we tested a larger domain with $R_\infty = 5R$ in a few cases with little effect on the result. We further assume mirror symmetry about the $r\theta$ plane such that the tensor $\mathbf{A}$ has the following form:

$$\mathbf{A} = \begin{pmatrix} A_{rr} & A_{r\theta} & 0 \\ A_{r\theta} & A_{\theta\theta} & 0 \\ 0 & 0 & 1 - A_{rr} - A_{\theta\theta} \end{pmatrix}. \tag{3}$$

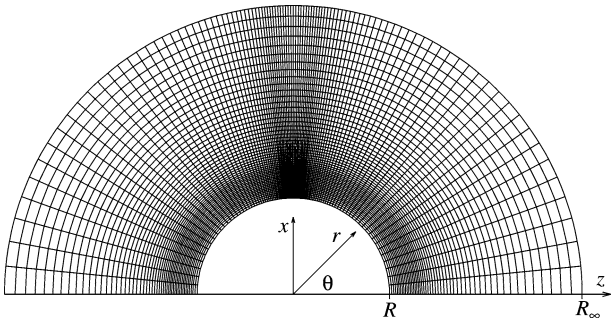

Fig. 2. The computational domain and a relatively coarse mesh with 51 and 101 grid points along r and θ, respectively.

By setting $A_{r\phi}$ and $A_{\theta\phi}$ to zero, we preclude twist in the solution. This turns out to be of little consequence as will be discussed in the next section after presenting the main results. A scalar order parameter is defined as $S = \sqrt{(3\mathbf{A}:\mathbf{A} - 1)/2}$ [29]. The anchoring condition is specified by a uniaxial $\mathbf{A}$ with the equilibrium order parameter S_{eq} and its major axis along the anchoring direction, which is radial at $r = R$ and along z at $r = R_\infty$. At $\theta = 0$ and π, we impose symmetry by $\partial A_{rr}/\partial\theta = \partial A_{\theta\theta}/\partial\theta = 0$ and $A_{r\theta} = 0$.

Since we are interested only in the final steady state, the temporal evolution of Eq. (2) is advanced explicitly, with time steps as large as numerical stability permits. The Laplacian $\nabla^2\mathbf{A}$ is discretized on a nonuniform rectangular grid (Fig. 2), which is adaptively refined during the evolution of $\mathbf{A}$ such that large spatial gradients at the defect are well resolved. Convergence with respect to grid size is confirmed by further refining the mesh after a steady state is reached. We use $\mathcal{L}$ as the characteristic length and $1/D_r$ as the characteristic time so the only dimensionless parameters in the problem are U and R. We fix $U = 4.94$ which corresponds to $S_{\text{eq}} = 0.6$ and vary R systematically. For each R, different initial configurations are used to explore multiple steady states.

To validate our numerical annealing scheme, we computed the hedgehog and line defects inside spherical and cylindrical enclosures with strong homeotropic anchoring. These simpler problems have been solved previously by Marrucci and coworkers using a self-consistency condition [30,31], which entails an additional approximation in expanding the exponential in the Boltzmann distribution into a Taylor series and truncating after the first order term. Our model avoids this problem by using the Bingham closure, which is exact in equilibrium. Considering this difference, our results agree generally well with theirs. Fig. 3 shows the radial profile of the order parameter $S(r)$ for the hedgehog defect. S vanishes at the center, where the material is isotropic, and grows monotonically toward $S_{\text{eq}} = 0.6$ at the enclosing spherical wall. Convergence with grid refinement is verified for both curves. The series truncation in reducing

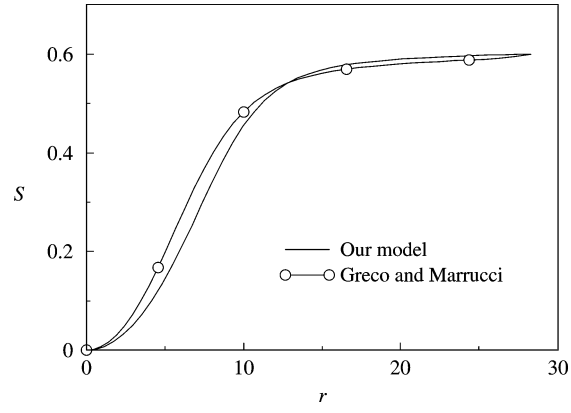

Fig. 3. Radial profile of the order parameter $S(r)$ in a hedgehog point defect computed using our method and the self-consistent condition of Greco and Marrucci [30].

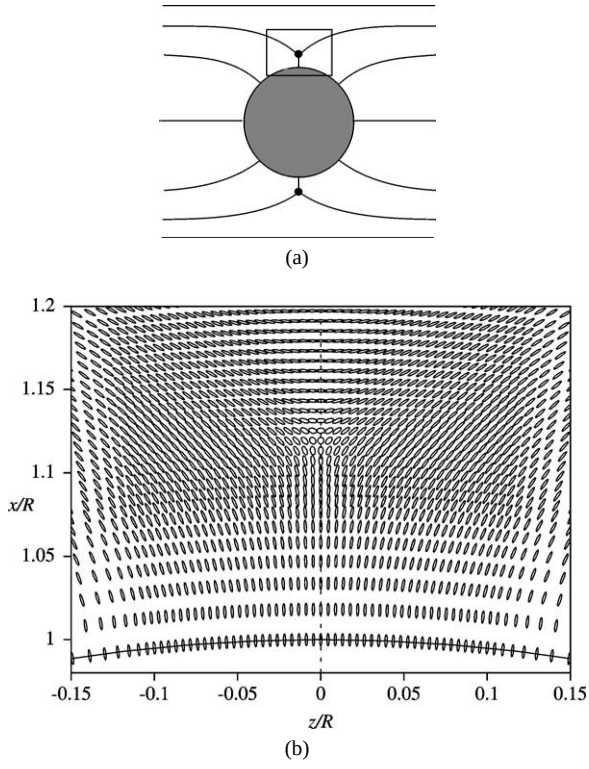

Fig. 4. Orientational pattern near the Saturn ring at $x = 1.128R$ for $R = 200$. The numerical result in (b) corresponds to the boxed area in the schematic (a) (see Fig. 2 for coordinate system). With three positive eigenvalues, **A** is represented by an ellipsoid whose projection is shown in the plot. The major axis of the ellipsoid gives the local director and its aspect ratio indicates the order parameter $S = \sqrt{(3\mathbf{A}:\mathbf{A} - 1)/2}$.

the self-consistent condition causes a small overprediction of S near the center and an underprediction farther out.

3. Results and discussion

Guided by previous studies [4,5,12], we have used three initial configurations: (a) a quadrupolar pattern that results from interpolating the anchoring conditions at R and R_∞ along the radius, with a "defect ring" on the equatorial plane; (b) a generalization of the dipolar ansatz of Lubensky et al. [2] intended to mimic the satellite defect, with the order parameter reduced near the defect; and (c) an intermediate configuration with a defect ring off the equatorial plane.

Starting from (a), the Saturn-ring pattern emerges for all R values tested: $15 \leqslant R \leqslant 40{,}000$, with a defect ring on the equatorial plane of the particle. An example is shown in Fig. 4 for $R = 200$. Except for the structured defect, the orientation field is qualitatively similar to predictions of the Frank theory [2,4,5]. At the very center of the defect, the ellipsoid representing **A** assumes a pancake shape, with two equal in-plane eigenvalues of 0.390 and a reduced order parameter $S = 0.170$. Away from the center, **A** becomes biaxial and S increases rapidly (Fig. 5). If we define the defect "core" as the area in which **A** is biaxial and S is significantly

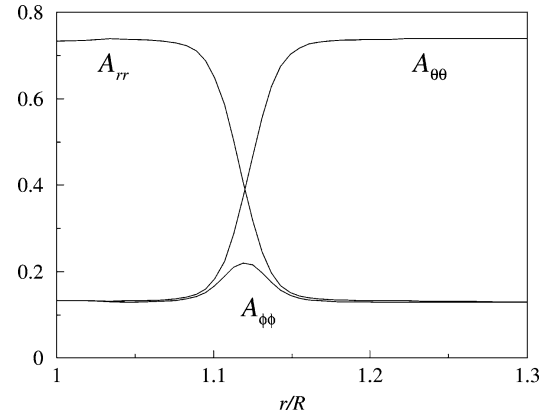

Fig. 5. Radial profiles of the three eigenvalues of **A** along $\theta = \pi/2$. The particle surface is at $r = R$ and the outer boundary is at $r = 3R$. Note that $A_{\phi\phi} = 1 - A_{rr} - A_{\theta\theta}$.

reduced, then Fig. 5 shows a very localized core with a radius of roughly $0.02R = 4\mathcal{L}$. Beyond $r \approx 1.3R$, not only has S returned to S_{eq}, but the orientation becomes more or less uniformly along z. Thus, when a particle is inserted into a nematic single crystal, its influence is rather limited; even the "strong anchoring" does not penetrate into the matrix beyond $0.3R$. As R increases, the Saturn ring shrinks gradually in relation to R, its radius r_d decreasing from $1.181R$ at $R = 15$ to $1.119R$ at $R = 40{,}000$. Previous calculations based on Frank elasticity and MD simulations have produced r_d values between $1.10R$ and $1.25R$ [4,5,12]. The MD work used a modified Gay–Berne potential with various parameters, and the Frank energy does not account for the intermolecular potential at all. Thus, the close agreement in r_d shows that this quantity is insensitive to the detailed physics. Experimentally, Gu and Abbott [8] reported that r_d/R decreases from 1.093 to 1.091 as R increases from 20 to 50 μm. The radius r_d is slightly below theoretical values, but its decrease with R is correctly predicted by the Frank theory [4,5] and our mean-field theory.

The main difference between our result and those based on MD and Frank elasticity is that we predict the Saturn ring on supramicrometer particles. The Frank theory with an assumed core radius of 10 nm predicts the Saturn ring to lose stability at $R = 720$ nm [4,5]. The MD simulations cannot access R larger than 15 times the molecular width. These lengths are much smaller than experimental values of $R \geqslant 20$ μm. The largest R for which we have computed the Saturn ring is $R = 40{,}000$. Since R is scaled by $\mathcal{L}$ which is roughly $1/10$ of the molecular length L, this corresponds to a particle radius of 8 μm for the 5CB used in experiments [8] with a molecular length $L \sim 2$ nm. In our simulations, the stability of the Saturn ring may extend well beyond $R = 40{,}000$. The defect core—the area in which S is significantly reduced—shrinks relatively with increasing R, and requires ever finer grids to resolve. Thus we did not strive to determine the upper limit of the Saturn ring regime. Stark [4,5] suggested that the close proximity of bounding walls in the experiment may have stabilized the Saturn ring. To

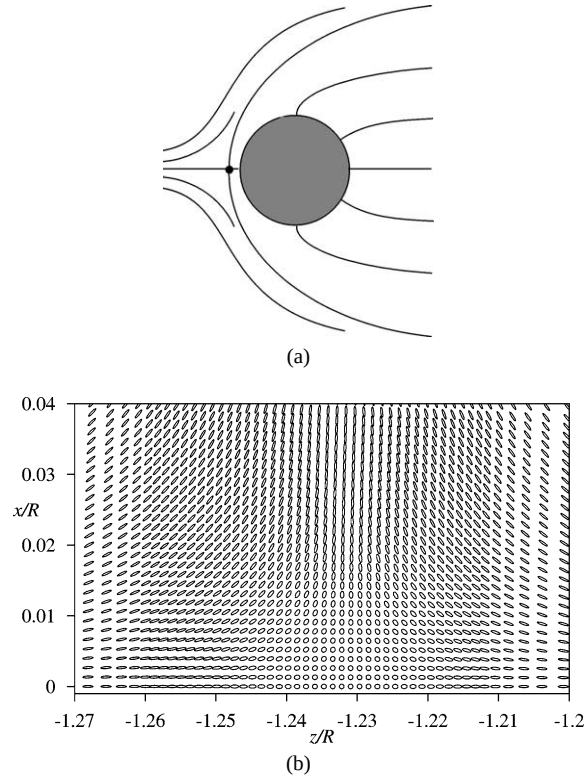

Fig. 6. The satellite point defect for $R = 500$. (a) Cartoon showing the orientational field near the particle–defect pair; (b) magnified view of the defect core constructed from our numerical solution.

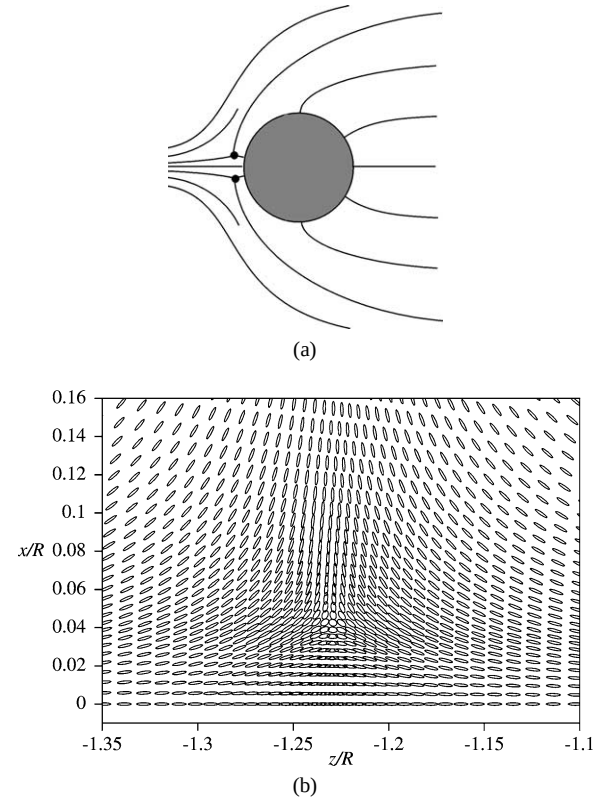

Fig. 7. The polar ring for $R = 300$. (a) Cartoon showing the orientational field around the particle and polar ring; (b) magnified view of the polar ring, at $(x, z) = (0.043, -1.23)R$, constructed from our numerical solution.

check the wall effect, we changed the position of the outer boundary from $1.5R$ to $5R$ with no apparent effects on the Saturn ring; this is consistent with the compactness of the defect noted above. An experimental and more direct test of Stark's suggestion remains to be done.

Starting from the initial configuration (b), we arrive at the satellite configuration if the particle radius $R \geqslant 150$. For smaller particles, the point defect opens into a ring, which then dilates and moves toward the equator to form a Saturn ring. We have computed the satellite defect up to $R = 20{,}000$ though it probably remains stable for all higher R. Fig. 6 shows the neighborhood of the point defect for $R = 500$. Away from the defect, the orientation field is similar to predictions of Frank elasticity [2]. The center of the defect is indicated by a vanishing S. With a finite mesh size, we locate the defect from the minimum of S, which is typically on the order of 10^{-3}. The distance from the point defect to the center of the particle is $z_d \approx 1.23R$ for all R tested. This compares with $1.22R$ to $1.25R$ predicted by the Frank theory, $1.4R$ by MD simulations, and $1.17R$ from experimental observations [1,4,5,12]. The experimental drops have diameters from 1 to 4 μm, which fall within the parameter ranges of this work and Refs. [4,5] but far exceed the size reachable by MD. The defect core in Fig. 6 is rather small, with a radius of approximately one molecular length L. This size does not vary appreciably for all R values that we tested. There is considerable biaxiality inside the core, but outside **A** is essentially uniaxial.

Starting from the intermediate initial configuration (c), the Saturn ring solution is recovered for $R \leqslant 160$, with the defect ring expanding and moving back to the equatorial plane. For larger particles, however, the ring achieves a stable equilibrium position near the pole of the particle. Fig. 7 shows this polar ring configuration for $R = 300$. As R increases, the polar ring shrinks toward the z axis; its radius decreases from $r_d = 0.127R$ for $R = 170$ to $r_d = 5 \times 10^{-4}R$ for $R = 20{,}000$ (Fig. 8). In dimensional terms, this corresponds to a reduction of r_d from $2.2L$ to L. Mesh refinement confirms that the polar ring, as a theoretical solution, persists without collapsing into a point defect. But for all practical purposes, we may consider the polar rings to merge into the satellite pattern at large R.

The polar ring pattern contradicts the prediction of the Frank theory that no stable configuration exists between the Saturn ring and the satellite solutions [4,5]. The MD simulations [12] did not find a polar ring regime, possibly because they used the Saturn ring or satellite pattern as initial condition from which the polar ring is unreachable for any R (cf., Fig. 9 below). Experimentally, Gu and Abbott [8] observed dipolar patterns with "a crumpled line," instead of a point defect, at the pole, and these defects coexist with the Saturn rings. This "ball of string" may be likened to our polar

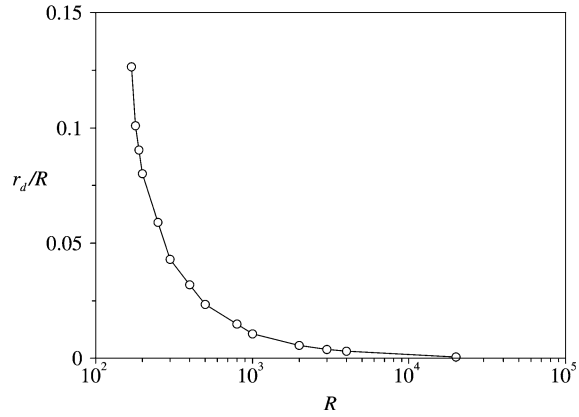

Fig. 8. Variation of the radius of the polar ring r_d with particle radius R.

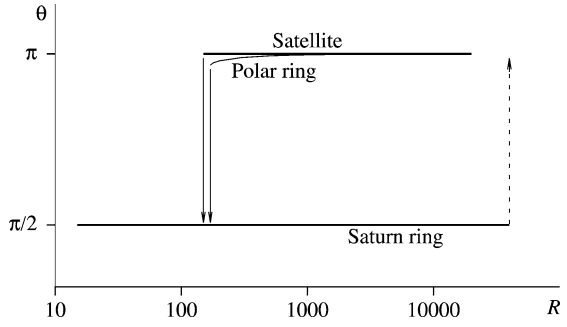

Fig. 9. Angular positions and stability ranges for the three types of defects. The transition from Saturn ring to satellite is hypothetical.

ring solutions but has a more complex structure. In addition, its length scale appears to be on the order of a micrometer, much larger than that predicted here.

Interestingly, the Landau–de Gennes energy predicts defect rings resembling our polar rings [10]. For sufficiently small R, these defect rings also open up into Saturn rings. With increasing R, however, the Landau–de Gennes defect ring maintains its radius and does not shrink into a hedgehog point defect. Based on this, Ref. [10] suggests that point defects do not exist in reality, and previously reported point defects are in fact rings. The discrepancy between our study and [10] regarding the existence of point defects may reflect the limitations of the Landau–de Gennes expansion as discussed in Section 2. But the ultimate verdict has to come from high-resolution experimental observations.

The three types of solutions have been obtained by assuming no twist (Eq. (3)). Stark [4,5] has explored twisted solutions using the Frank theory. He showed that a twist transition may occur for the satellite configuration if the twist constant is sufficiently weak, and that no twisted solution exists with elastic isotropy. The latter result, along with the fact that no experimental evidence for the twisted solution has been published, motivated us to use the simple twist-free $\mathbf{A}$ in Eq. (3). It is of interest, however, to see whether our tensor-based solutions are stable against twist. Thus, we solve the evolution equation (2) with the full tensor $\mathbf{A}$, which now has five independent components. The previous twist-free solutions with Saturn rings, satellite defects or polar rings are used as the initial condition, with a spatially random disturbance imposed on the $A_{r\phi}$ and $A_{\theta\phi}$ components. In other words, $A_{r\phi}$ and $A_{\theta\phi}$ at different grid points are assigned random numbers between zero and an upper bound p. We have tested only small values of $p \leqslant 10^{-2}$ since larger ones may violate the positive definiteness of $\mathbf{A}$. For these, the disturbances die away in subsequent evolution, confirming the linear stability of the twist-free solutions. Of course, this does not rule out the existence of twisted solutions reachable from entirely different initial conditions. The limitation to accessing individual metastable states is inherent to the simulated annealing approach.

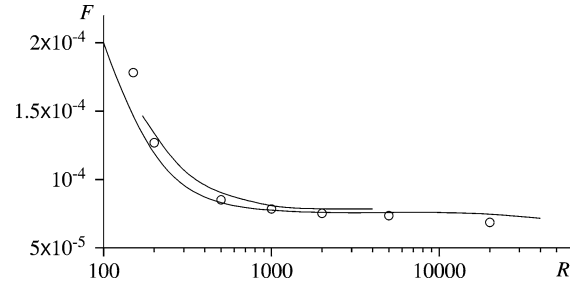

Fig. 10. The total free energy for the three defect patterns. F is scaled by νkT times the total volume of the liquid crystal. The upper curve is for the polar ring, the lower curve is for the Saturn ring, and the data points are for the satellite defect.

To sum up, multiple stable orientation patterns may be reached from different initial conditions, and a "phase diagram" has been constructed in Fig. 9. The Saturn ring is observable for R ranging from molecular dimensions to micrometers. The satellite defect is stable for R greater than about 15 molecular lengths. From proper initial configurations, the polar ring pattern can be realized for an intermediate R range. Though the upper bound of the Saturn ring regime is not determined, the ring will probably contract into a satellite defect once it loses stability at large R. Such a scenario is suggested by experiments [8]. When the satellite defect becomes unstable at small R, it expands into a Saturn ring rather than a polar ring; the critical particle radius $R \approx 150$ is too small for the polar ring to be stable.

While "the question of which of the states has the lower energy cannot be answered unambiguously" by the Frank theory [7], the mean-field theory affords us an opportunity to address that. Using Eq. (1), the free energy density is written as [31]

$$f(\mathbf{r}) = -\nu kT \ln Z + \frac{3}{4}\nu kT U(\mathbf{A} + \mathcal{L}^2\nabla^2\mathbf{A}) : \mathbf{A} - f_0,$$

where Z is the partition function and f_0 is f evaluated using the equilibrium $\mathbf{A}$ without spatial variation. A volume integration of f gives the total free energy F, which is then scaled by νkT times the volume and plotted in Fig. 10 for the three types of solutions. The small magnitude of the dimensionless F does not imply dominance by thermal fluctuation. Rather, it is due to the fact that the particle distorts the nematic orientation only within a small volume in its

neighborhood. This "short-range" behavior has been noted for the Saturn ring (Fig. 4) but prevails in the other regimes as well. In all cases, F decreases with increasing R because the defect core shrinks in relation to the entire domain. For smaller R, the Saturn ring has the lowest energy, while for larger R, the satellite configuration is the global attractor. A crossover occurs between $R = 1000$ and 2000. The polar ring always costs the most energy except for perhaps the lowest R. Which state prevails in an experiment depends strongly on the distortion and deformation history of the sample.

In conclusion, the mean-field theory provides a self-consistent description of orientational defects near a colloidal particle immersed in a nematic medium. In particular, it predicts the Saturn ring to persist on supramicrometer particles, and a polar ring to arise from appropriate initial conditions. These new results appear to be consistent with experiments. We must also note the limitations of this work. The Marrucci–Greco potential (Eq. (1)) assumes that the spatial variation occurs over length scales much larger than the interaction length $\mathcal{L}$. Thus, we approach the limit of the mean-field theory's validity with defect cores on the order of the molecular length $L \sim 10\mathcal{L}$. Besides, we have assumed elastic isotropy and strong anchoring, and neglected surface terms in the free energy including the saddle-splay term [4,5]. Future work will relax these restrictions and apply the mean-field theory to particle interaction and self-assembly in nematic dispersions.

Acknowledgments

This work was supported in part by the National Science Foundation (CTS-0229298, CTS-9984402, PHY-9907949) and the National Natural Science Foundation of China (Grant 20174024). The authors thank Davide Hill, Harley Klein, Francesco Greco, and Morton Denn for helpful discussions and an anonymous referee for suggesting the calculations to test the stability of the solutions against twist.

References

[1] P. Poulin, H. Stark, T.C. Lubensky, D.A. Weitz, Science 275 (1997) 1770.
[2] T.C. Lubensky, D. Pettey, N. Currier, H. Stark, Phys. Rev. E 57 (1998) 610.
[3] E.M. Terentjev, Phys. Rev. E 51 (1995) 1330.
[4] H. Stark, Eur. Phys. J. B 10 (1999) 311.
[5] H. Stark, Phys. Rep. 351 (2001) 387.
[6] O.V. Kuksenok, R.W. Ruhwandl, S.V. Shiyanovskii, E.M. Terentjev, Phys. Rev. E 54 (1996) 5198.
[7] R.W. Ruhwandl, E.M. Terentjev, Phys. Rev. E 56 (1997) 5561.
[8] Y. Gu, N.L. Abbott, Phys. Rev. Lett. 85 (2000) 4719.
[9] O.V. Sozinova, D.A. Hill, presented at the Annual Meeting of Society of Rheology, Bethesda, MD, October 2001.
[10] J.I. Fukuda, M. Yoneya, H. Yokoyama, Phys. Rev. E 65 (2002) 041709.
[11] J.L. Billeter, R.A. Pelcovits, Phys. Rev. E 62 (2000) 711.
[12] D. Andrienko, G. Germano, M.P. Allen, Phys. Rev. E 63 (2001) 041701.
[13] G. Marrucci, F. Greco, Mol. Cryst. Liq. Cryst. 206 (1991) 17.
[14] L. Onsager, Ann. N.Y. Acad. Sci. 51 (1949) 627.
[15] W. Maier, A. Saupe, Z. Naturforsch. A 13 (1958) 564.
[16] M. Doi, S.F. Edwards, The Theory of Polymer Dynamics, Oxford Univ. Press, New York, 1988.
[17] R. Kupferman, M.N. Kawaguchi, M.M. Denn, J. Non-Newtonian Fluid Mech. 91 (2000) 255.
[18] J.J. Feng, G. Sgalari, L.G. Leal, J. Rheol. 44 (2000) 1085.
[19] C.V. Chaubal, L.G. Leal, J. Rheol. 42 (1998) 177.
[20] J. Feng, C.V. Chaubal, L.G. Leal, J. Rheol. 42 (1998) 1095.
[21] M. Doi, J. Chem. Phys. 79 (1983) 5080.
[22] A. Sonnet, A. Kilian, S. Hess, Phys. Rev. E 52 (1995) 718.
[23] F. Greco, Mol. Cryst. Liq. Cryst. 290 (1996) 139.
[24] P.G. de Gennes, Phys. Lett. A 30 (1969) 454.
[25] J. Katriel, G.F. Kventsel, G.R. Luckhurst, T.J. Sluckin, Liq. Cryst. 1 (1986) 337.
[26] A. Poniewierski, T.J. Sluckin, Mol. Phys. 55 (1985) 113.
[27] B.J. Edwards, A.N. Beris, M. Grmela, J. Non-Newtonian Fluid Mech. 35 (1990) 51.
[28] G. Sgalari, L.G. Leal, J.J. Feng, J. Non-Newtonian Fluid Mech. 102 (2002) 361.
[29] R.G. Larson, The Structure and Rheology of Complex Fluids, Oxford Univ. Press, New York, 1999.
[30] F. Greco, G. Marrucci, Mol. Cryst. Liq. Cryst. 210 (1992) 129.
[31] I. Sigillo, F. Greco, G. Marrucci, Liq. Cryst. 24 (1998) 419.